

Measurements and modeling of acoustic scattering from partially and completely buried spherical shells

A. Tesei,^{a)} A. Maguer,^{b)} and W. L. J. Fox^{c)}

SACLANT Undersea Research Centre, Viale San Bartolomeo 400, 19138 La Spezia, Italy

R. Lim

Coastal Systems Station/Dahlgren Naval Surface Warfare Centre, Code R21, 6703 West Highway 98, Panama City, Florida 32407-7001

H. Schmidt

Department of Ocean Engineering, MIT, Cambridge, Massachusetts 02139

(Received 27 August 2001; revised 28 May 2002; accepted 29 July 2002)

The use of low-frequency sonars (2–15 kHz) is explored to better exploit scattering features of buried targets that can contribute to their detection and classification. Compared to conventional mine countermeasure sonars, sound penetrates better into the sediment at these frequencies, and the excitation of structural waves in the targets is enhanced. The main contributions to target echo are the specular reflection, geometric diffraction effects, and the structural response, with the latter being particularly important for man-made elastic objects possessing particular symmetries such as bodies of revolution. The resonance response derives from elastic periodic phenomena such as surface circumferential waves revolving around the target. The GOATS'98 experiment, conducted jointly by SACLANTCEN and MIT off the island of Elba, involved controlled monostatic measurements of scattering by spherical shells which were partially and completely buried in sand, and suspended in the water column. The analysis mainly addresses a study of the effect of burial on the dynamics of backscattered elastic waves, which can be clearly identified in the target responses, and is based on the comparison of measurements with appropriate scattering models. Data interpretation results are in good agreement with theory. This positive result demonstrates the applicability of low-frequency methodologies based on resonance analysis to the classification of buried objects. © 2002 Acoustical Society of America. [DOI: 10.1121/1.1509425]

PACS numbers: 43.30.Jx, 43.40.Fz, 43.20.Tb [DLB]

I. INTRODUCTION

At the high frequencies traditionally used for mine countermeasures (MCM), typically in excess of 30 kHz, the acoustic scattering by moderate-sized bottom targets (~ 1 m) is well described by the geometrical theory of diffraction. The reason for using these high frequencies is the strong dependence of prevailing technology on imaging resolution for detection, and more importantly, for classification. However, it is well established that at lower frequencies, man-made targets in particular may support the excitation of strong structural waves or resonances consistent with their structural symmetries. For target sizes ~ 1 m, these resonances can be strongly excited in the 1–10 kHz frequency regime, well below the frequencies required for classification by imaging.

Analysis of wave scattering by underwater elastic objects in the $4 < ka < 30$ range (where k is the acoustic wave number and a is the characteristic dimension of the object) has identified several target classifying features that are reflected in the scattering, e.g., the radius, the wall thickness,

and the elastic properties for spherical shells.^{1,2} However, the question is whether features based on the spatial and temporal characteristics of the structural response can provide robust and reliable classification clues. If they can, this will provide a technology push for including lower-frequency sonars in operational systems.

Another benefit of moving to lower sonar frequencies is the improved seabed penetration. For insonification above the seabed critical grazing angle (assuming a flat seabed), the attenuation decreases approximately linearly with frequency, while below the critical grazing angle, the evanescent lateral wave field in the bottom penetrates deeper.³ Also, the reverberation from surficial features such as small-scale sand ripples will decrease with decreasing frequency, with an increase in signal-to-reverberation as a result.⁴

Here, a coordinated experiment and modeling effort explores the potential of low- to medium-frequency sonar concepts for improved target detection and classification. Specifically the analysis aims at verifying through direct comparison of experimental data and wave theory scattering models whether the circumferential waves backscattered by an elastic, axisymmetric target remain detectable and identifiable whether the target is proud or buried. Further, the analysis evaluates how the burial depth, the sediment properties, and the seabed interface influence the dynamics of the generated structural responses.

^{a)}Electronic mail: tesei@saclantc.nato.int

^{b)}Present address: Thales Underwater Systems, 274 Victoria Road, Rydalmer NSW 2116, Australia.

^{c)}Present address: Applied Physics Laboratory, 1013 NE 40th St., Seattle, WA 98105-6698.

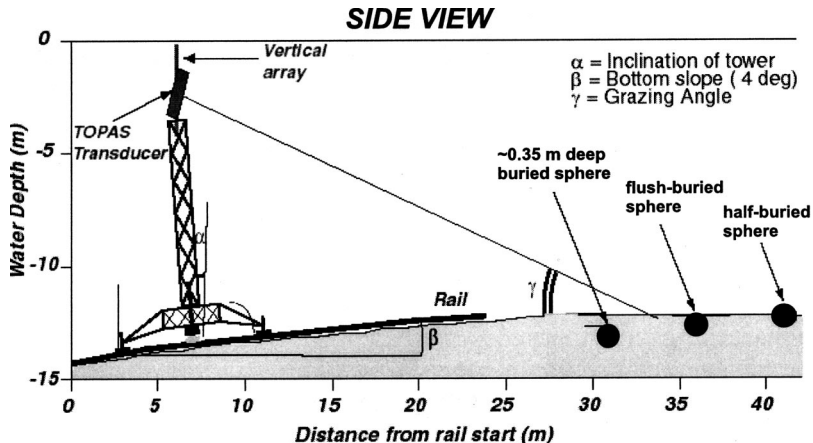


FIG. 1. GOATS'98 experimental configuration.

Past experimental and modeling work has provided evidence for the excitation of structural waves in completely buried spherical shells, including investigations on the sensitivity to burial depth, sediment type, and grazing angle.^{5,6} The excitation of target resonances for flush and partially buried targets has more recently been investigated using new modeling capabilities,^{6,7} but equivalent experimental work has been lacking.

The analysis presented here uses the comprehensive data set acquired during the GOATS'98 experiment.⁸ Monostatic and bistatic measurements were conducted on a suite of man-made targets of different shapes and burial depths. The targets were insonified by a parametric projector that scanned over a wide range of grazing angles from below critical to above. This paper will be limited to the analysis of back-scattering with insonification above critical grazing for three identical spherical shells: one half buried, one flush buried, and one completely buried. The spherical shells were relatively thin-walled and filled with air. Hence, the free-field scattering physics is relatively simple to model and well understood.^{9–11} The analysis will use the suite of scattering models presented in Refs. 5–7.

II. EXPERIMENTAL CONFIGURATION

The GOATS'98 experiment⁸ was carried out in May, 1998, on a sandy bottom in 12–15 m water near Marciana Marina, off the island of Elba, Italy. The TOPAS (Topographic Parametric Sonar) source was used to insonify the targets with a highly directional beam. The sonar is an end-fire parametric array of 24 horizontal staves. It covers the frequency range 2–16 kHz for the secondary frequency and 35–45 kHz for the primary frequency. The transmitting source level is about 238 dB re: 1 μ Pa at 1 m for the primary frequency and the source level obtained at the difference frequencies varies from 190 to 207 dB re: 1 μ Pa at 1 m (see Ref. 12). A short single pulse is obtained by transmitting a weighted burst at the primary frequency. At the secondary frequency the vertical beamwidth is 3°–5° and the horizontal is about 8°. As with all parametric sonars, there are no conventional sidelobe structures, and the beam pattern decays monotonically outside the main 3 dB down beamwidth. The far field is estimated to start at about 30–35 m in front of the transducer, while the volume of nonlinear interaction¹³ is es-

timated to extend for the first 11 m (see Ref. 3). All the measurements were at ranges larger than the nonlinear interaction length of the sonar, so that nonlinear penetration effects can be ignored in the data analysis.

The experimental configuration is shown in Fig. 1. In order to acquire data from various source-receiver geometries, the transmitter was mounted on a 10 m tower. The tower in turn was mounted on a 24 m linear rail on the bottom, along which its position could be precisely controlled. The TOPAS transmitter was mounted in a pan-and-tilt assembly so that the transmission direction could be accurately measured. A linear receiving array of 16 equally spaced omnidirectional hydrophones was mounted vertically in a near-monostatic configuration. The array was designed to work at 8 kHz; hence, the distance between adjacent elements is 0.094 m generating an acoustic aperture of 1.41 m. The main lobe of its beam pattern is about 6° at 8 kHz, 26° at 2 kHz, and 3° at 15 kHz. The sidelobes are more than 13 dB lower than the main lobe. The sensitivity of all the hydrophones was approximately constant (around –163 dB) in the bandwidth 1–15 kHz.

Three identical spherical shells were deployed in line with the TOPAS rail at different burial depths (about 35 cm into the sediment, flush, and half-buried). One of the shells was measured before burial under quasi-free-field conditions suspended in the water column. They were air-filled, steel spherical shells nominally of 0.53 m outer radius and 3 cm wall thickness. As the relative thickness h (defined as the ratio between wall thickness, d , and outer radius, a) was equal to 0.0566, they are classified as thin (though others may consider this an intermediate thickness¹⁴ tending to thin). They had a steel lug at the top which was used for suspension and transportation. The spherical shells were constructed by welding two hemispherical shells together. The nonuniformity of the resulting shell at the weld point was not measured, and could be a source of unknown acoustic effects in the following results.

Iospeed conditions were measured in the water column at 1520 m/s. The depth of the water over the target field was about 12 m. Grain size estimates of the bottom corresponded to medium sand. The average density of the sediment, measured over the volume of bottom cores, was 1.91 g/cm³. The sediment propagation loss was estimated around 0.5 dB/λ, as demonstrated in Refs. 3 and 15. Sound speed was estimated

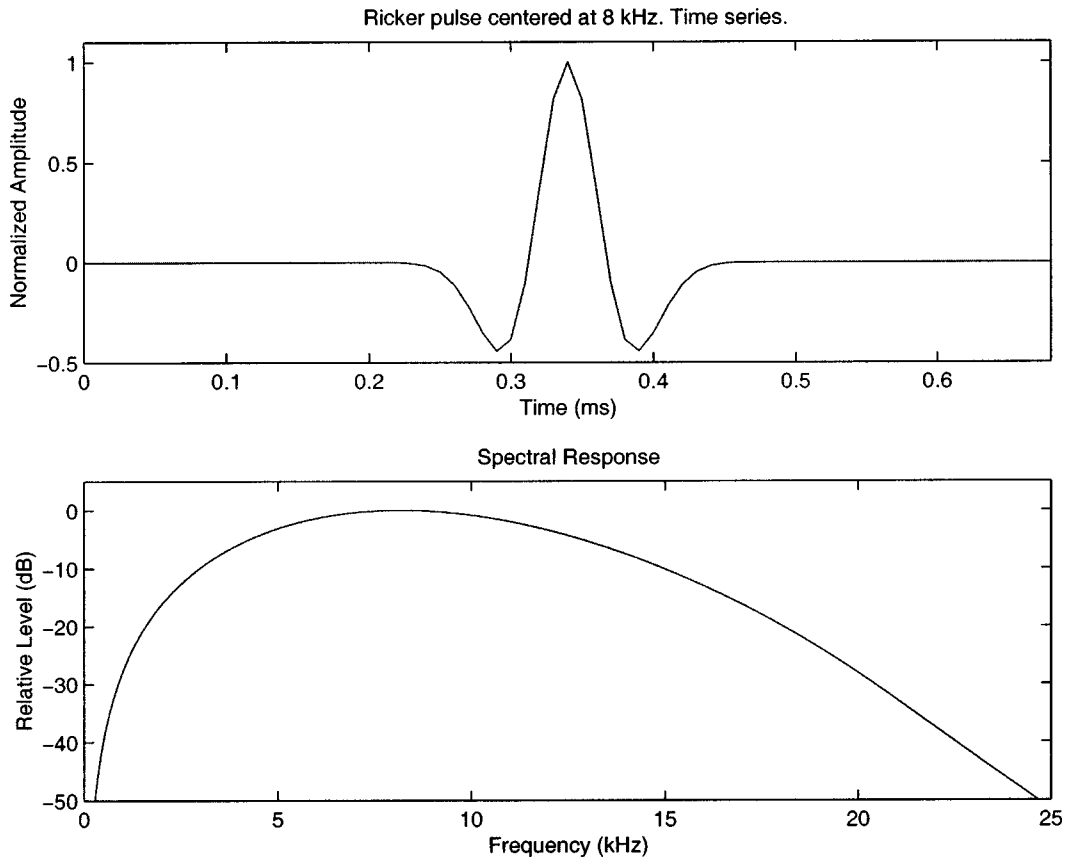


FIG. 2. Model of a Ricker pulse centered at 8 kHz.

to be on the order of 1720 m/s by pulsed travel time measurements on sediment cores centered at 200 kHz. However, the analysis of low-frequency sound waves emitted by the TOPAS and received on a vertical array of buried hydrophones in the immediate vicinity of the GOATS'98 target field has proved the strong dispersion of acoustic waves in a sandy seabed.¹⁵ From those acoustic measurements the sediment sound speed was estimated to be approximately 1640 m/s at 8 kHz. This dispersion is consistent with the predictions of Biot's theory for propagation in porous media. These considerations also influence the estimation of the sediment critical angle which should consequently decrease as the frequency is reduced; thus, the nominal critical angle of the sediment is estimated at 28° from the measurements on cores at 200 kHz and at 22° if a sound speed of 1640 m/s is assumed.

III. TARGET SCATTERING MODELS

Scattering models for a spherical shell either in the free field (i.e., suspended in the water column) or buried in the seabed are briefly presented. Models are developed in the frequency domain and provide the scatterer transfer function. In order to compare simulated and real sonar data in the time domain, the simulations of the transfer function are multiplied in the frequency domain by the model of the incident pulse transmitted by the acoustic source, and the resulting products are inverse Fourier transformed.¹⁶ A Ricker function, defined as the second derivative of a Gaussian,¹⁷ is used for the incident pulse at a nominal center frequency of 8 kHz

(Fig. 2). The time signal is normalized to unit peak amplitude and its spectral level is normalized to 0 dB maximum. The simulations are computed to a maximum frequency of 25 kHz, but the results are presented in the bandwidth 0–15 kHz and then analyzed between 2 and 15 kHz, where the signal-to-interference ratio of the at-sea data is sufficient to allow model-data comparison and elastic wave analysis. In the simulated and measured target scattering response plots, the time series will be normalized with respect to the maximum amplitude of the specular echo, and the signal spectral levels will be normalized to 0 dB maximum.

A. Spherical shell in free field

The free field case is used as for comparison of the results obtained when the spherical shells are partially or completely embedded in the sediments. Under free field conditions, the acoustic pressure p_s scattered by an elastic fluid-filled spherical shell, insonified by an incident plane wave with acoustic pressure $p_i = p_0 e^{i(kr - \omega t)}$, can be presented in a series form:¹⁸

$$p_s = p_0 e^{-i\omega t} \sum_{n=0}^{\infty} i^n (2n+1) A_n h_n^{(1)}(kr) P_n(\cos \theta), \quad (1)$$

where p_0 is the pressure amplitude of the incident wave, k is the wave number, r is the range, θ is the scattering direction angle, n is the modal order, $h_n^{(1)}$ is the spherical Hankel function of n th order, A_n are coefficients to be determined from the boundary conditions,¹⁸ and P_n is the Legendre polyno-

mial of n th order. The scattered field can be also expressed in terms of the form function $F(\theta)$:

$$p_s = p_i \left(\frac{a}{2r} \right) F(\theta), \quad (2)$$

where a is the spherical shell's outer radius. In the far field (i.e., for $r \rightarrow \infty$), the backscatter ($\theta = \pi$) form function $F(\pi)$, expressed as a sum of partial waves $F_n(\pi)$, becomes

$$F(\pi) = \sum_{n=0}^{\infty} F_n(\pi) = \frac{2}{ika} \sum_{n=0}^{\infty} (-1)^n (2n+1) A_n. \quad (3)$$

Scattering effects due to excitation of elastic waves on the shell are analyzed in terms of wave speed dispersion curves. The phase ($c_{ph,n}$) and group ($c_{g,n}$) speeds of the n th modal frequency f_n of a circumferential wave, taking a path of radius R , are defined, respectively, as¹⁸⁻²⁰

$$\begin{aligned} |c_{ph,n}| &= \frac{2\pi R f_n}{n + 1/2}, \\ c_{g,n} &= 2\pi R (f_n - f_{(n-1)}). \end{aligned} \quad (4)$$

In the low- to medium-frequency range, for thin air-filled spherical shells, the elastic contribution to scattering is due to the lowest-order flexural and compressional waves of the shell. These waves may be considered as the generalization of Lamb waves on a flat plate⁹ for the case of a curved plate.

The symmetric (or compressional) S_0 *Lamb-type wave*^{10,20} is supersonic, almost nondispersive, and travels in the shell with phase and group speeds almost coinciding and asymptotically tending to the shell material membrane speed, c_{shell}^* . It reradiates at each revolution with an angle corresponding to the shell material coupling angle:

$$\theta_c^* = \arcsin \left(\frac{c_{ext}}{c_{shell}^*} \right), \quad (5)$$

where c_{ext} is the sound speed in the medium loading the shell. The dynamics and energetic contribution to backscattering of this wave is expected to be only slightly influenced by the object outer medium (or media).

The antisymmetric (or flexural) A_0 *Lamb-type wave* of a spherical shell in vacuum bifurcates into two dispersive waves upon fluid loading. Of the two, the wave that more strongly influences the acoustic scattering amplitude of the target is the subsonic A_{0-} *Lamb-type wave*.^{10,21} At low frequencies (until its phase speed approaches the outer-medium sound speed at the so-called coincidence frequency, f_c), it is flexural in nature,²¹ and the effect of fluid loading on its dynamics is essentially inertial. In this frequency region it is only slightly influenced by the outer-medium properties, like the S_0 wave. Around the coincidence frequency the so-called midfrequency enhancement occurs as a result of trace velocity matching²² when the flexural wave phase speed approaches that of the exterior diffractive field. In the midfrequency enhancement region the shell response amplitude reaches its maximum at the coincidence frequency. The A_{0-} wave starts to behave like a fluid-borne wave, becoming difficult to detect with increasing frequency because increased

radiation damping makes it harder for the wave to travel all the way around the shell to radiate significantly in the back direction. Around the coincidence frequency it reradiates at each revolution approximately along the tangent to the sphere cross section. Its group speed reaches its maximum at the coincidence frequency. Hence, at frequencies around and beyond the coincidence frequency the A_{0-} wave dynamics and energy level are strongly influenced by the speed of sound in the exterior.

Around the coincidence frequency the A_{0-} wave is phase-coupled with the other antisymmetric Lamb-type wave, namely the A_{0+} *Lamb-type wave*,^{10,20} the nature of which is opposite to the A_{0-} wave,²¹ as for frequencies lower than the coincidence frequency it is fluid-borne and highly dispersive, hence highly radiation damped and almost undetectable. When its phase speed approaches the external sound speed, it changes nature from fluid-borne to flexural (shell-borne). Beyond the coincidence frequency the A_{0+} wave becomes supersonic and less dispersive, hence more easily detectable from backscattered data.

Figure 3 shows the simulated response of a water-loaded spherical shell to a Ricker pulse centered at 8 kHz. The interpretation of the simulated data is shown in terms of S_0 , A_{0-} , and A_{0+} wave echoes in time and resonance modes in frequency. Here and in the following analysis, the modeled and measured spherical shells have the same nominal elastic parameters (steel compressional speed $c_p = 5950$ m/s, shear speed $c_s = 3240$ m/s, membrane speed $c_{steel}^* = 5435$ m/s, density $\rho = 7.7$ g/cm³), the density of the sea water is set to 1 g/cm³ and its sound speed is set to the measured value 1520 m/s.

In order to maintain high signal-to-reverberation levels even in the case of buried targets, the data analysis focuses on a low- to intermediate-frequency range that stops approximately at the end of the region of midfrequency enhancement, hence extending over a bandwidth where the S_0 and A_{0-} waves are more easily detectable and only a few modes of the A_{0+} wave can be identified (as shown in Fig. 3). As a consequence, only the S_0 and A_{0-} waves will be considered in the following. Figure 4 shows the travel paths followed by the S_0 and A_{0-} Lamb-type waves revolving around the spherical shell in the free field. For thin-walled spherical shells the radius R of the circumferential wave path corresponds to the shell outer radius a for both the S_0 and the A_{0-} waves:

$$R_{S_0} = R_{A_{0-}} = a. \quad (6)$$

A simple empirical formula, which was shown²³ to be valid for steel, aluminum, and similar materials, allows the approximate estimation of the sound speed in the external medium loading the shell, c_{ext} , from f_c and the shell wall thickness d :

$$c_{ext} \approx f_c 2\pi d. \quad (7)$$

This expression is related to the classical observation that the peak of the midfrequency enhancement on thin spherical shells scales with a constant frequency-thickness product. It will be used in lieu of local measurements of c_{ext} around the shell, which can be difficult in buried underwater configura-

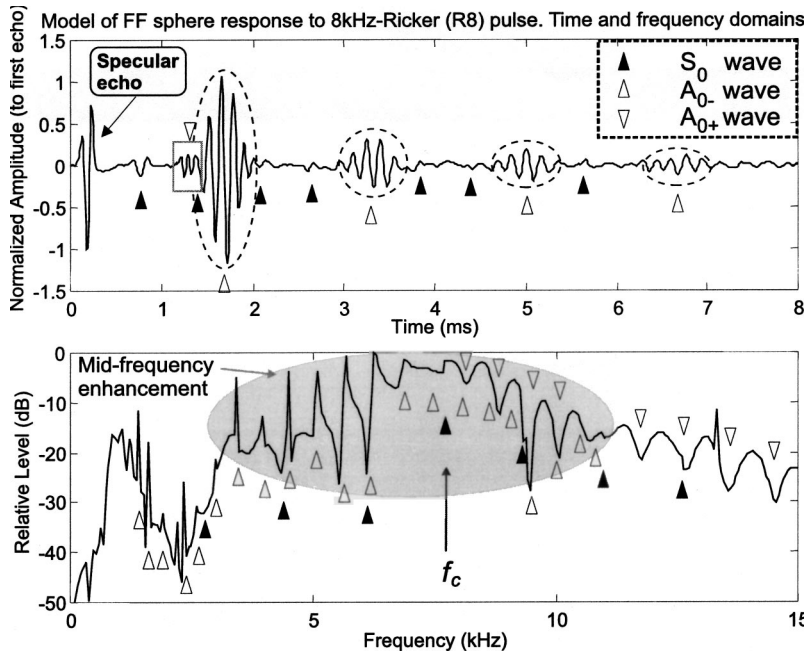


FIG. 3. Model of backscattering by free-field spherical shell. Elastic scattering analysis is applied.

tions. The viability of this approximation will be discussed in the following analysis.

B. Partially and completely buried spherical shells

Measurements of the fully and partly buried spherical shells are compared with model predictions based on transition- ($T-$) matrix solutions for the scattered field.^{5,7} These solutions assume the bottom to be fluid with a flat water/sediment interface. While this assumption may not be strictly satisfied in the measurements, it is expected to provide better predictions of the scattering response than ignoring the environmental layering. The basic solutions are generalizations of the free-field spectral solution given by Boström^{24,25} and take the form:

$$\begin{aligned} \mathbf{u}^{\text{sca}}(\mathbf{r}) &= \sum_{j=1}^N \sum_{pml} \Psi_{pml}(\mathbf{r} - \mathbf{d}^{(j)}) \gamma_{pml}^{(j)} \\ &= \sum_{j=1}^N \sum_{pml} \sum_{p'm'l'} \Psi_{pml}(\mathbf{r} - \mathbf{d}^{(j)}) \\ &\quad \times \mathbf{T}_{pmlp'm'l'}^{(j)} \alpha_{p'l'm'}(\mathbf{r}_s). \end{aligned} \quad (8)$$

The field scattered by an obstacle embedded in N ($N \geq 1$) layers of a plane-stratified environment is formulated as a sum over a contribution from the segment in each layer. An $e^{-i\omega t}$ steady-state time dependence is assumed but suppressed. The T matrix of the obstacle segment penetrating the j th of the N host layers in contact with the obstacle is defined with the second equality as the operator, $\mathbf{T}^{(j)}$. It projects the vector of incident field coefficients, $\alpha(\mathbf{r}_s)$, onto the vector of expansion coefficients, $\gamma^{(j)}$, for the field scattered by the segment contained in layer j . Special basis sets defined in Ref. 26, $\Psi_{pml}(\mathbf{r} - \mathbf{d}^{(j)})$, satisfying the host's boundary conditions and centered on each segment at $\mathbf{d}^{(j)}$, are used to expand the scattered field. The incident field coefficients for a point source at \mathbf{r}_s are also proportional to this basis, i.e., $\alpha_{pml}(\mathbf{r}_s) \propto \Psi_{pml}(\mathbf{r}_s)$.²⁶ Directional vertical line sources can

be modeled by multiplying these coefficients by a phase factor to steer the beam with and applying a simple integral over the length of the source.⁵ Using this basis to express the fields external to the scatterer, transmission through the seabed to and from the scatterer is properly accounted for.

One can accommodate an obstacle with a layered core such as a steel shell by expressing $\mathbf{T}^{(j)}$ via the following matrix formula:

$$\begin{aligned} \mathbf{T}^{(j)} &= -[\hat{\mathbf{L}}^{(j)}(\hat{\mathbf{D}} + \mathbf{T}^0 \mathbf{D})^{-1}(\hat{\mathbf{E}} + \mathbf{T}^0 \mathbf{E}) - \hat{\mathbf{M}}^{(j)}] \\ &\quad \times [\mathbf{L}(\hat{\mathbf{D}} + \mathbf{T}^0 \mathbf{D})^{-1}(\hat{\mathbf{E}} + \mathbf{T}^0 \mathbf{E}) - \mathbf{M}]^{-1}, \end{aligned} \quad (9)$$

where the matrices $\hat{\mathbf{D}}$, $\hat{\mathbf{E}}$, \mathbf{L} , $\hat{\mathbf{L}}^{(j)}$, \mathbf{M} , and $\hat{\mathbf{M}}^{(j)}$ are as defined in Ref. 26 and the matrices \mathbf{D} and \mathbf{E} differ from $\hat{\mathbf{D}}$ and $\hat{\mathbf{E}}$, respectively, only in replacing regular partial-wave functions with outgoing ones. The interior structure of the obstacle is contained in \mathbf{T}^0 , the free-field scattering T matrix of the core embedded in an unbounded elastic medium specified with the material parameters of the outer layer of the obstacle. Thus, $\mathbf{T}^0 = \mathbf{0}$ if the obstacle is homogeneous. The form of \mathbf{T}^0

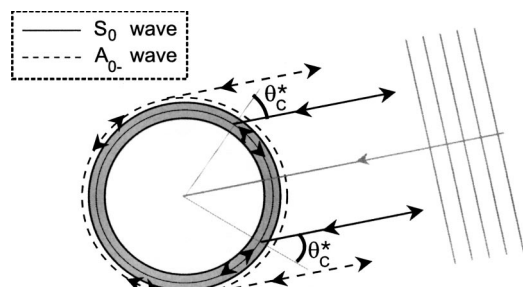


FIG. 4. Simplified scheme of travel paths for the S_0 and A_{0-} Lamb-type elastic waves backscattered by an air-filled spherical shell around the coincidence frequency. The ray diagram is based on the ray theory approximation for fluid-loaded elastic objects (Refs. 20 and 33). The travel path of the A_{0-} wave is drawn outside the shell in order to emphasize its fluid-borne nature around the coincidence frequency. The reradiation angles are outlined for the two wave types. The wall thickness is not in scale.

has been presented previously for elastically layered cores²⁷ as well as fluid cores.²⁸ When $N=1$, Eqs. (8) and (9) reduce to the formulation presented in Ref. 5 for fully buried obstacles. Translation operators may be used to extract from the **L** and **M** matrices terms that make up the rescattering matrix evident in the solution of Ref. 5. The rescattering matrix accounts for multiple interactions of the scatterer with the interfaces of the environment. For the present applications, we leave these interaction terms embedded in the **L** and **M** matrices to mitigate convergence problems that arise with partial burial configurations.

While the segmented *T*-matrix formulation contained in Eqs. (8) and (9) may be used to calculate the field scattered by layered inhomogeneous obstacles that penetrate a plane-layered host, the obstacle layering should be sufficiently smooth and obey certain convergence restrictions. In particular, for surface fields expanded in basis functions of spherical geometry, the origin-centered sphere that circumscribes the inner boundary of each homogeneous obstacle layer should never overlap the origin-centered sphere that inscribes its outer boundary. This restriction becomes a problem for elongated shells but the acoustic response of spherical shells can be calculated effectively.

For comparisons with measurements, Eqs. (8) and (9) were implemented using the numerical techniques described in Ref. 26. All surface and wave number integrations needed to evaluate the basis functions and the *T* matrix were performed by applying 32 point Gauss quadrature to a sufficient number of segments of the specified integration contours to attain a stable, converged result. Matrix products involving inversions were performed with Gaussian elimination. Double precision complex arithmetic was used in all calculations. A resolution of 400 frequency points was maintained in the predicted spectra and the scattered field at each frequency point was evaluated with a maximum truncation of 50 l and m values. The field calculations are scaled by the in-water source amplitude at 1 m. Only one bottom layer was assumed ($N=1$).

A simplified scheme of the travel paths of the S_0 and A_{0-} elastic waves around the coincidence frequency is shown in Fig. 5 in the case of partial burial, which is the most complicated geometry. Under partial burial conditions, the reradiation angle for each wave in either medium can vary with the shell coupling, i.e., as the outer-medium sound speed varies, trace velocity-matching^{20,22} determines the point at which the incident field couples to the shell and, consequently, the reradiation angle.

Theoretically,^{5,7} the S_0 wave is not expected to be greatly influenced by burial, except for a slight shift toward lower frequencies of its first resonance modes, due to the significantly greater inertial loading of the shell in the sediment, having a larger relative density than water. The shift is expected to be more evident for the first mode and to decrease as the modal order (and frequency) increases. Further, the frequency shift should increase with the percentage of target surface in contact with sediment. The A_{0-} wave is expected to behave like the S_0 wave at low frequencies, where it is subject to inertial loading. Therefore, its first free-field modes should also tend to shift to lower frequencies. As

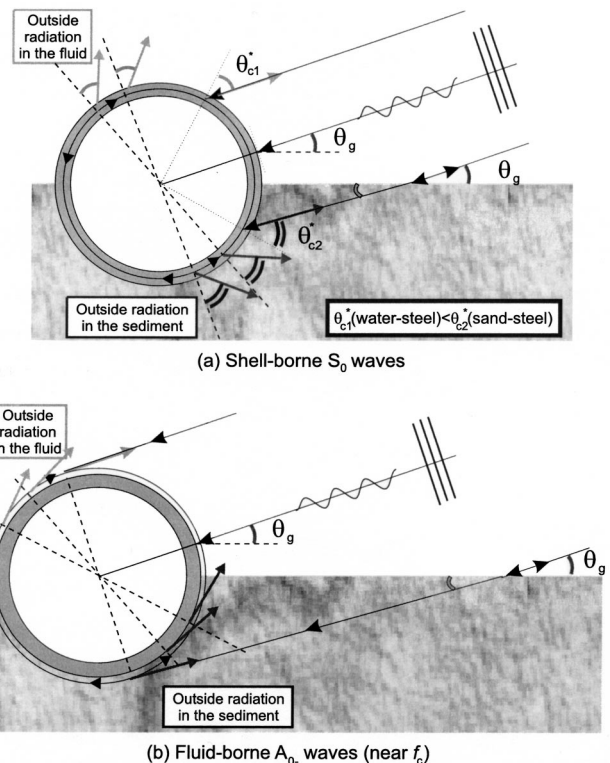


FIG. 5. Simplified travel paths of the shell-borne S_0 (a) and fluid-borne A_{0-} (b) waves in the case of partial burial. As in Fig. 4 the travel path of the A_{0-} -wave is drawn outside the shell in order to emphasize its fluid-borne nature around the coincidence frequency. The wall thickness is not in scale.

the A_{0-} wave becomes fluid-borne in nature, its phase speed increases to approach the exterior sound speed, which is higher when the target is completely buried. From Eq. (4), this means the modes of the A_{0-} wave that are excited in a midfrequency enhancement, as well as the coincidence frequency f_c , are expected to experience an upward shift upon burial. For partial burial, we hypothesize that these modes will again shift an amount consistent with the percentage of target surface in contact with sediment.

In line with the above-given expectations, we will treat the target exterior as an effective homogeneous medium if the shell is partially buried so that the exterior sound speed and exterior density needed to determine wave dispersion on the shell can be easily specified. Thus, an effective exterior sound speed $c_{\text{ext}}^{\text{eff}}$ is determined by generalizing Eq. (7) as

$$c_{\text{ext}}^{\text{eff}} \approx f_c 2 \pi d. \quad (10)$$

This assumption should be reasonable if the dominant contribution to the backscatter from the S_0 and A_{0-} waves are from complete circumnavigations of the shell, i.e., contributions from paths around the shell that include reflections at the interface are small. Under these circumstances, $c_{\text{ext}}^{\text{eff}}$ may be expected to be comparable to a weighted harmonic average of the sound speeds of the two exterior fluids in order to account for propagation of the exterior diffracted field through both fluids.²⁹

Similarly, an external effective density $\rho_{\text{ext}}^{\text{eff}}$ will be defined in the case of partial burial as an average of the densities of the two external fluids, weighted according to the fraction of the volume of the sphere loaded by each fluid.

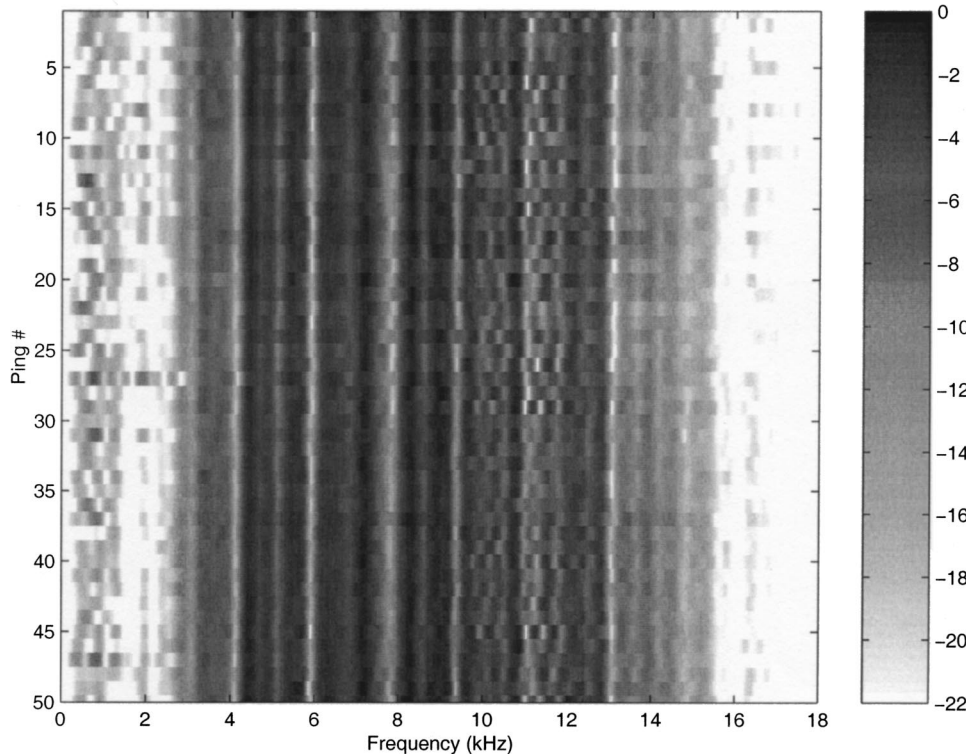


FIG. 6. Typical example of ping-to-ping fluctuation of the measured data sets. Spectrum of the 50 pings scattered from the deeply buried target.

This definition of effective density is particularly appropriate at low frequency, where the more significant impact of inertial (i.e., mass) loading suggests a weighting based on mass fraction (density multiplied by volume fraction).

Of course, these effective parameters are not meant to represent the environment in the scattering calculations for a partially buried shell. They will be used only in the algorithm outlined in the Appendix for determining the dispersion of surface guided waves on the shell from the measured or calculated backscatter signals. These definitions for $c_{\text{ext}}^{\text{eff}}$ and $\rho_{\text{ext}}^{\text{eff}}$ are convenient because they allow the determination of the dispersion properties as if the environment of the shell were homogeneous. The result should be understood to be an estimate of the average dispersion of the A_{0-} and S_0 waves experienced upon propagation around the buried and unburied sections of the shell. The rationale for expecting the resulting dispersion curves to be representative of the average dispersion is based on the intuitive expectation that the timing and coupling of waves going around the shell at any point on its surface depends on the local exterior parameters at that point only. Therefore, the time for a wave to go around the top of the shell in water is independent of the time it takes going around the bottom in the sediment. In an analogous fashion, for a pulse transmitted through layers of materials of different speed, one can determine the transmission time by summing the thickness/sound-speed ratios of each layer or treat the stack of layers as a single layer with an effective sound speed given by a harmonic average of the layer sound speeds. Both treatments give identical results for the pulse transmission time. As in that simple example, both definitions for the effective parameters in our problem have been found to yield good results in simulation.

IV. EXPERIMENTAL RESULTS

The data selected are the aligned coherent averages of 50 pings of the beamformed acquisitions by the vertical array. From a preliminary analysis of ping-to-ping data fluctuation over each data set, the measurement variability was estimated. As a typical example of the studied data sets, Fig. 6 shows the ping-to-ping variability of the spectrum of the response measured from the deeply buried spherical shell. The signal appears stable in the bandwidth 2–15 kHz, whereas below 2 kHz the signal is almost completely hidden by noise and, consequently, data analysis cannot be applied. In particular, in the range 2–15 kHz, the standard deviation of the location of the dips or peaks, corresponding to the resonance frequencies of the generated elastic waves, was estimated to be approximately 1%–3% of the mean value. As a consequence, the aligned coherent average can be used in this range for data analysis as a robust measurement of each target response.

The geometry of each measurement was selected in such a way that the target could be completely illuminated by the TOPAS central beam. However, while the free-field target could be measured in the far field of the source so that the far-field model presented in Sec. III A is applicable, the proud and buried targets were measured in the near field of the TOPAS. As the T -matrix model described in Sec. III B can simulate directional sound beams in the near field of the source, the TOPAS vertical beam pattern was approximated by the beam pattern of a linear vertical array with a 5°-wide main lobe in the applications of the model to these cases. Despite the imperfect simulation of the actual TOPAS beam pattern, the T -matrix model should provide the correct target response in terms of the resonance frequency locations and

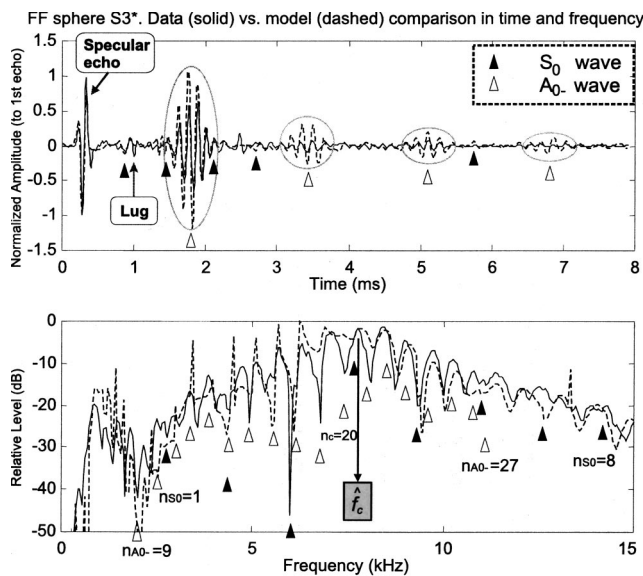


FIG. 7. Free-field spherical shell. Model-data comparison in time and frequency domains. Elastic scattering analysis by identification of S_0 and A_{0-} -wave echoes in time and resonance modes in frequency. Resonance frequency modes are labeled by n_{S0} and n_{A0-} , respectively.

radiation damping of the elastic waves. However, a mismatch with the scattering amplitude can be expected.

A. Free field spherical shell (FF)

The spherical shell suspended in midwater was measured at a range of about 35 m, which was in the far field of the source and uniformly illuminated notwithstanding the high directivity of the TOPAS. The measured target response is presented in Fig. 7, where comparison with the computed model is outlined and the elastic wave analysis is superimposed. Model-data agreement is generally good in terms of signal shape, levels, and feature identification, except for an evident mismatch in the level of the A_{0-} wave features. In the frequency domain, a mismatch in the level of most of the measured A_{0-} resonance modes and a decay of about 5 dB of the midfrequency enhancement are estimated with respect to expectation. A corresponding mismatch is also evident in all the A_{0-} wave echoes in the time domain. The sharpness of the A_{0-} resonance features is reduced in the data spectrum, probably as a result of signal time windowing.³⁰ However, the broader mismatch in the levels of the midfrequency enhancement in frequency and of the wave echoes in time is likely caused by nonuniformities of the shell wall thickness and/or by the presence of the steel lug attached to the top of the target. The same effects will be seen also in the following, particularly in the model-data comparison of data from half- and flush-buried spherical shells.

Further, two arrivals recorded in the data time series at about 1 and 2.5 ms, respectively, were not predicted by the model. On the basis of geometrical considerations the first echo corresponds to the time of arrival predicted for the top lug of the spherical shell; the second remains unidentified.

At low frequency ($f < 2$ kHz) the model-data fit is poor, as the data spectrum is 5–10 dB lower than the model prediction. This may be explained if the TOPAS transmitted a Ricker pulse with a low-frequency component lower than

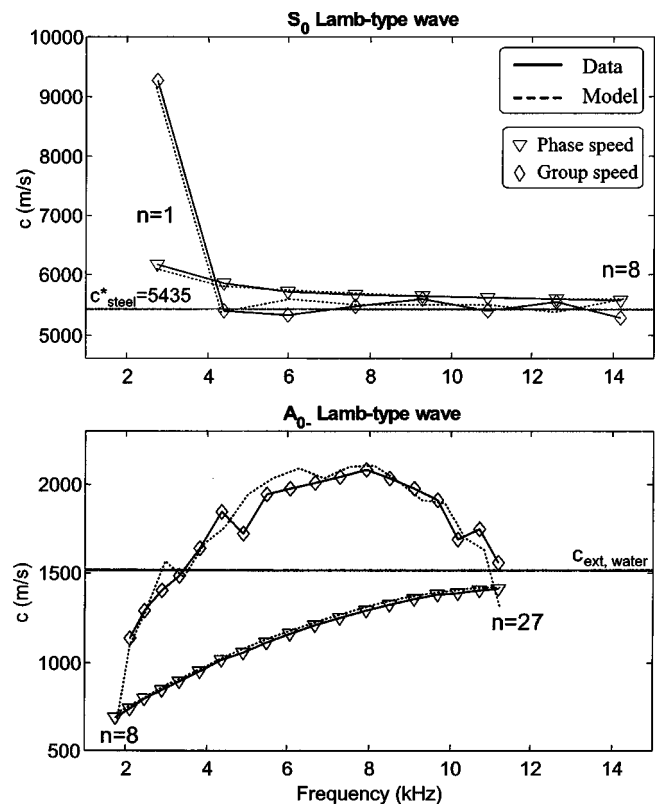


FIG. 8. Free-field spherical shell. The S_0 (top) and A_{0-} (bottom) wave dynamics is described by phase and group dispersion curves.

expected by the ideal wave form shown in Fig. 2 and used for simulations. This possibility is suggested by the high ping-to-ping variability below 2 kHz in Fig. 6. However, this hypothesis cannot be confirmed by measurements because the direct echo transmitted by the source could not be recorded under the same geometry and by the same system used for measuring the target. A low-frequency mismatch will be seen in the following model-data comparisons for all the cases considered.

The modeled and estimated dynamics of the S_0 and A_{0-} -waves are compared in Fig. 8 by means of the respective dispersion curves, which have been computed from the identified wave modes (labeled n) according to the formulas in Eq. (4). The wave dynamics are in good agreement with theory for both waves. Also, unlike the scattering amplitude, wave dispersion appears quite insensitive to shell imperfections even in the case of the A_{0-} wave.

The S_0 and A_{0-} wave modes are extracted in the frequency domain, and identified on the basis of model-data comparison. The approach used here and in the following for the extraction and identification of resonance frequencies from data is described in the Appendix.¹ The estimated coincidence frequency, \hat{f}_c , is localized at 8.12 kHz by the peak of the envelope of the spectral midfrequency enhancement, which roughly corresponds to the maximum of the A_{0-} wave group speed curve.¹ By using Eq. (7) the estimated sound speed in water is 1530 m/s, which is in good agreement with the measured value of 1520 m/s.

HB sphere S3. Data (solid) vs. model (dashed) comparison in time and frequency

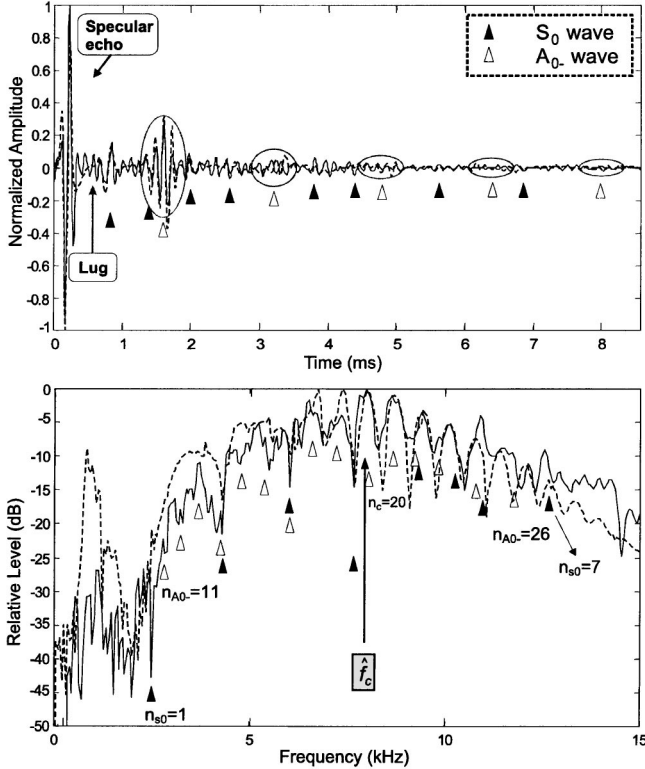


FIG. 9. Half-buried spherical shell. Model-data fit and elastic scattering interpretation.

B. Half-buried spherical shell (HB)

In Fig. 9 the measured response from the half-buried (HB) spherical shell is compared with the T -matrix-based simulation described in Sec. III B. The measured grazing angle is about 26° and the range 22 m. The best fit is obtained for a burial depth of 10.6 cm below the sphere equator and a sand sound speed set to 1647 m/s. This result is in agreement with the theoretical predictions of a reduced speed in the porous media as frequency is reduced, demonstrated by the at-sea data analysis¹⁵ mentioned in Sec. II.

This case is the most complicated to interpret, due to the presence of two outer media (i.e., water and sand). However, both the waves are still identified in time and in frequency and have relative levels comparable with the free-field case. The mismatch in the level of the wave, which was noticed in the free-field data analysis, is much less evident here in the time domain and in the midfrequency enhancement. This is probably the result of a more optimal orientation of the shell. (In tank tests with welded spherical shells, it has been observed that echo amplitudes due to the A_{0-} wave are significantly affected by the orientation of the equatorial weld relative to the incident wave.) However, the mismatch noticed at low frequency (i.e., for $f < 2$ kHz) in the free-field data as discussed previously is even more significant here. The reason for the larger discrepancy is unknown.

Above 13 kHz the model-data fit is poorer because of an enhancement of the reverberant noise, which superimposes several unmatched echoes on the predicted target response in the time domain. Among those unpredicted echoes, one, localized in Fig. 9, should correspond to the return from the

FB sphere S2. Data (solid) vs. Model (dashed) comparison in time and frequency

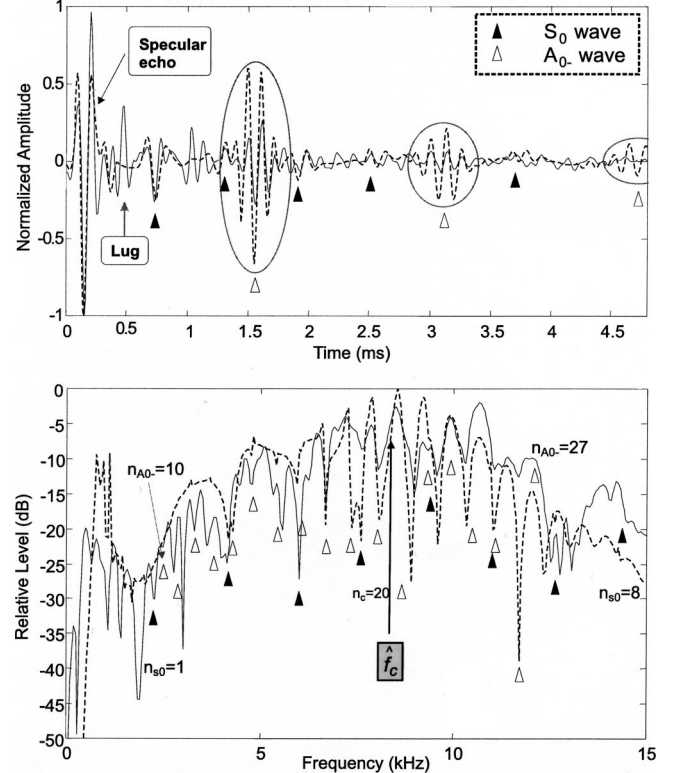


FIG. 10. Flush-buried spherical shell. Model-data fit. Elastic scattering analysis.

target's support lug, but its level is unexpectedly low relative to the specular echo when compared to that measured in the free field.

From \hat{f}_c localization ($\hat{f}_c = 8.25$ kHz), the estimate of the effective external sound speed obtained from Eq. (10) is 1555 m/s, which is not far from the result (1580 m/s) obtained by applying the formula of c_{ext}^{eff} proposed in Ref. 29. This result validates the hypothesis that even when the A_{0-} wave becomes fluid-borne in nature, it continues to revolve around the whole spherical shell and is not limited to travel only in water, reflected back by the bottom boundary. This effect might also be a result of the relatively small impedance difference between water and sand.

C. Flush- and deeply-buried spherical shells (FB/DB)

The response of the flush-buried spherical shell is plotted in Fig. 10, where it is compared with the simulated data and analyzed in terms of elastic wave extraction and identification. The measured grazing angle is 34.5° and the range is 18 m. The best fit model for the flush-buried spherical shell corresponds to a burial depth of 2 cm from the top of the target, and sand sound speed set to 1642 m/s.

As shown in Fig. 10, both the waves outlined in free-field data are evident and their scattering levels relative to the specular echo are comparable with the free-field case. The mismatch in the A_{0-} wave levels is particularly evident in the time domain. As in the previous data, a strong mismatch is evident at low frequency. Above 13 kHz the model-data fit is poor because of a significant decrease of the signal-to-reverberation level, hence the elastic scattering analysis be-

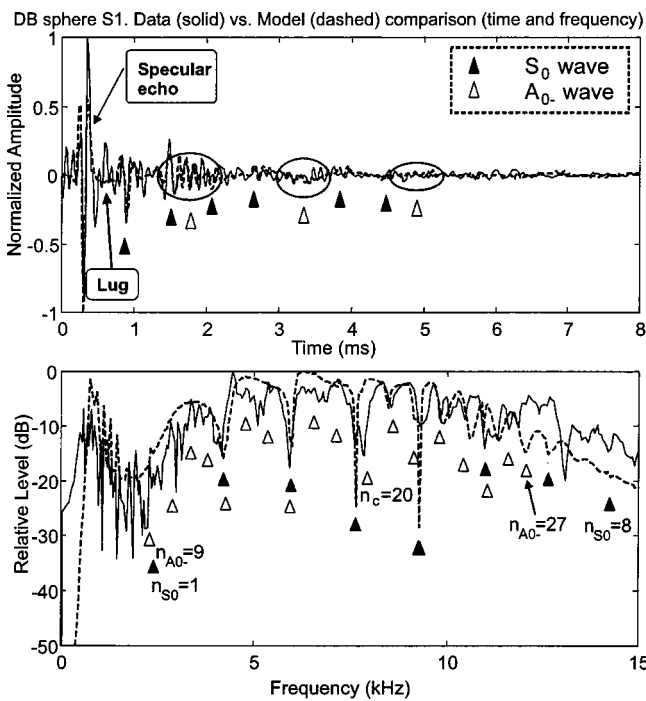


FIG. 11. Deeply-buried spherical shell. Model-data fit. Elastic scattering analysis.

comes unreliable. This effect is more evident than in the half-buried case, in which the signal is maintained at a higher level by the scattering contribution from the water-loaded part of the target. The reverberation, which may be due mainly to volume inhomogeneities, affects the data time series with several unmatched echoes. The strong return following the specular echo is identified as a reflection by the shell's support lug. Its considerably strong level is justified by the relatively short travel path through the sediment needed to account for this echo. From \hat{f}_c localization ($\hat{f}_c = 8.765$ kHz), Eq. (7) provides the outer medium speed estimate of 1652 m/s.

For the measurements of the deeply buried spherical shell, the grazing angle is about 42° and the range is about 16 m. The best fit with the model was found by setting the burial depth to 35 cm from the top of the target and the sand sound speed to 1652 m/s. Figure 11 shows the model-data comparison in time and frequency and the superimposed analysis of elastic waves. As in the flush-buried case, the fairly strong arrival from the top lug can be easily identified on the basis of geometrical considerations. Its level, being comparable to the predicted elastic wave contribution, is justified by the relatively short path length through the sediment needed to account for it.

As expected from theory, the level of the S_0 wave remains essentially unchanged with respect to the specular echo as the burial depth varies. Therefore, the S_0 echoes and resonance modes are easily identified. However, due to the attenuation caused by propagation through the sand, the A_{0-} wave level decreases significantly with respect to the flush-buried case. The low signal-to-interference ratio only allows a subset of these resonance modes to be unambiguously identified in the frequency domain. The significant increase of the reverberation level is already evident at 12 kHz and

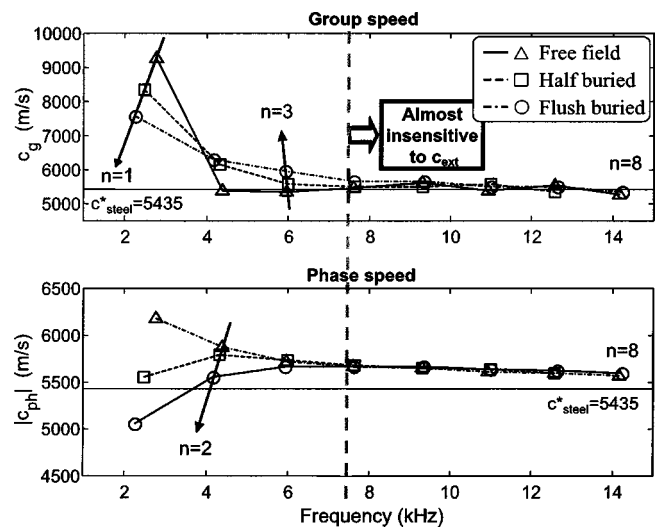


FIG. 12. Comparison of S_0 wave dispersion curves as the burial depth changes, for the free-field, half-buried, and flush-buried cases. The estimated resonance modes are localized on the respective curves by triangles, squares, and circles.

causes many spurious echoes to appear in the data time series with levels comparable to the predicted elastic response of the target. Under these conditions the midfrequency enhancement cannot be detected and localized with sufficient precision to allow a robust estimation of the coincidence frequency.

Further, a model-data mismatch appears at low frequencies. Here, the discrepancy is less severe than in the half-buried and flush-buried cases, but it is of the same order (5–10 dB) as that measured in the free field. Nevertheless, it is notable that the sand sound speed values that result in good agreement between the scattering models and data for both the flush-buried and deeply buried spherical shells are very close to each other and to that selected in the half-buried case. When compared to the sand sound speed measured in core samples (1720 m/s) by transmitting a 200 kHz pulse, there is a significant difference. As outlined in Sec. IV B, this result confirms those presented in Ref. 15.

D. Analysis of elastic wave dynamics

The behavior of elastic waves *versus* frequency as burial depth changes is predictable using the simple theoretical arguments described in Sec. III B. The elastic analysis is performed in terms of the wave speed dispersion curves estimated from the averaged data presented for each target in Secs. IV A–IV C. For supercritical insonification at ranges beyond the nonlinear volume interaction region of the parametric source, the selection of different grazing angles and ranges for measurements on the three buried targets is not expected to influence the characteristics of the generated elastic waves in terms of resonance frequencies. Hence, the data sets are assumed comparable.

Due to the robustness of the scattering measurements discussed in Sec. IV, the deviation of the dispersion curves of the S_0 and A_{0-} waves estimated from each ping is small compared to the mean values on each data set (for both waves, the standard deviations on the phase speed range

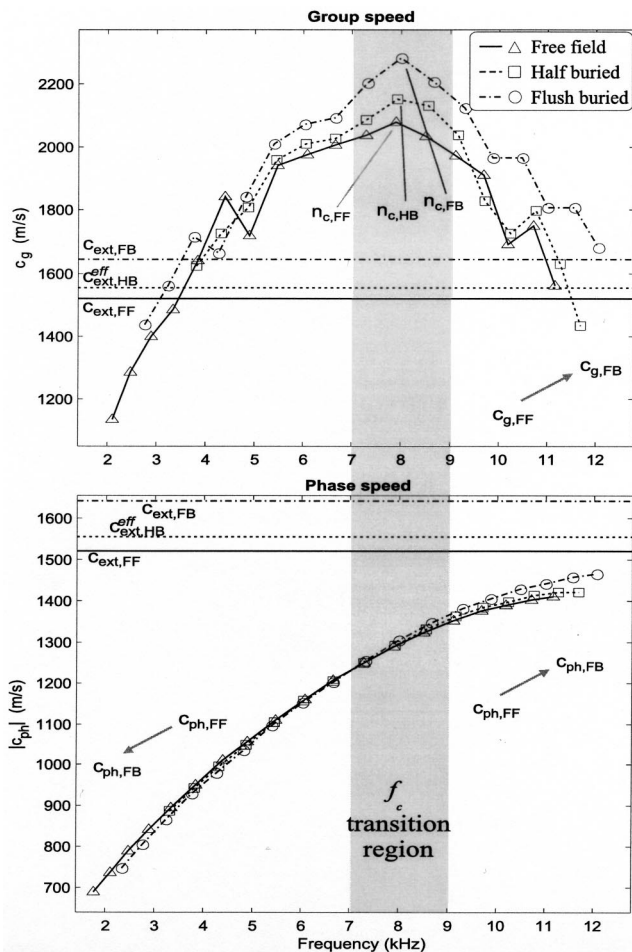


FIG. 13. Comparison of A_{0^-} wave dispersion curves among the free-field, half-buried, and flush-buried cases. The estimated resonance modes are localized on the respective curves by triangles, squares, and circles. The gray bar localizes the transition region around the coincidence frequency where the A_{0^-} wave is expected to change its nature from a shell-borne to a fluid-borne wave.

from 2 to 6 m/s from target to target, on the group speed from 30 to 90 m/s). As a result, the dispersion curves for individual pings are quite close to those estimated from ping averaged data. Given the data stability in the range 2–15 kHz and the number of pings (50) averaged in each data set, the estimation of the dispersion curves computed from the averaged data sets is assumed to be statistically consistent.

The dispersion curves of the waves estimated in the free-field, half-buried, and flush-buried cases are compared in Figs. 12 and 13. These three cases are compared first in order to analyze the wave dynamics as the percentage of shell surface loaded by the sediment changes from 0 to 100. Due to the very small standard deviations computed on the estimated dispersion curves, the comparison among curves belonging to different burial cases can be considered statistically significant. The smoothness of the experimental curves that will be shown in the following helps confirmation of the robustness of their estimation.

As emphasized by the arrows in Fig. 12, the first three modes (but particularly the first one) of the S_0 wave shift down in frequency with burial depth, from the free field to the totally buried case, which is a consequence of the pre-

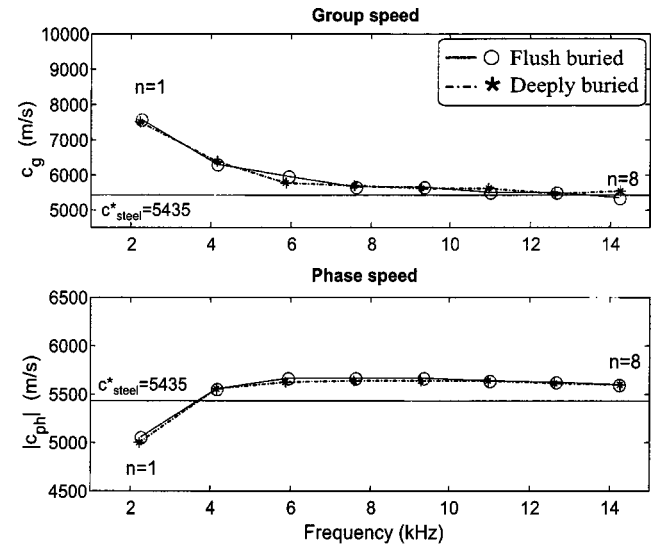


FIG. 14. Comparison of S_0 wave dispersion curves as the burial depth changes between the flush-buried and deeply buried cases. The estimated resonance modes are localized on the respective curves by circles and stars.

dicted greater inertial loading caused by sand compared to water. For higher frequencies, dispersion due to the sediment becomes negligible in all cases; hence, all three curves almost coincide and tend to the membrane speed for steel, c_{steel}^* .

In accordance with theory, the phase speed of the A_{0^-} wave has opposite trends at frequencies lower and higher than the coincidence frequency, while the group speed increases with burial across the whole bandwidth. At low frequency, where the wave behaves as shell-borne, its modes tend to shift to lower frequencies due to sand inertial loading (as noticed for the first S_0 modes). As the percentage of surface area loaded by sediment increases, these modes exhibit a larger shift down in frequency. Consequently, the wave phase speed tends to decrease. A concurrent increase of the group speed is observed at these frequencies because sediment loading shifts the resonance modes more as the mode order decreases causing the frequency gap between modes to increase with burial.

Around and beyond the coincidence frequency, where the wave behaves as a fluid-borne wave, the wave characteristics are opposite, namely the A_{0^-} mode locations shift to higher frequencies and the phase speed tends to increase with burial depth and frequency. Also the group speed increases with burial and frequency because, at higher frequencies, the upward shift of the resonance modes again widens the gap between the modes. This is expected from theory. The shift to higher frequency is related to the increased speed of the effective outer medium in which this wave travels as the burial depth increases. At the same time, the whole midfrequency enhancement region shifts up with burial, together with the coincidence frequency, which is linearly related to the effective external sound speed according to the empirical formula of Eq. (10).

In Figs. 14 and 15 the S_0 and A_{0^-} wave dynamics are analyzed as the burial depth changes between two cases of completely buried spherical shells. Between the flush-buried and deeply buried cases the changes in wave dynamics are

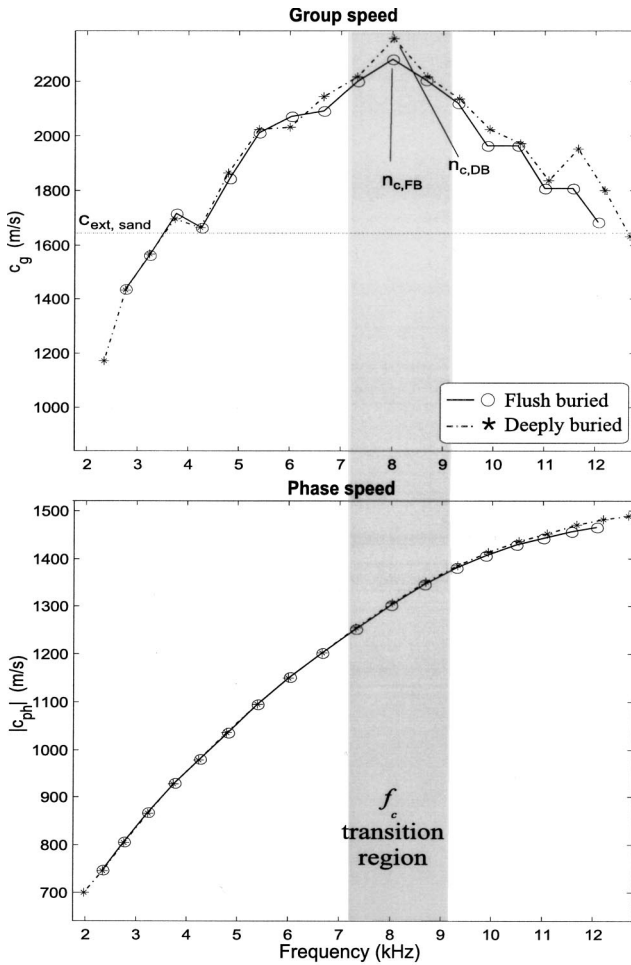


FIG. 15. Comparison of A_{0-} wave dispersion curves between the flush-buried and deeply buried cases. The estimated resonance modes are localized on the respective curves by circles and stars. As in Fig. 13, the gray bar localizes the transition region around the coincidence frequency where the A_{0-} wave is expected to change its nature from a shell-borne to a fluid-borne wave.

slight, as expected,⁵ and the respective phase and group speeds of the S_0 and A_{0-} waves almost coincide. In particular, a minute low-frequency shift of the first S_0 and A_{0-} modes of the deeply buried shell is predicted by theory⁵ with respect to the flush-buried one, due to an increasing effective inertial mass loading of the shell as its distance from the water-sand boundary increases. However, this effect is detectable only in the first and third modes of the measured dispersion curves of the S_0 wave, and cannot be resolved for the A_{0-} wave. The frequency shifts are expected to be so small that the measurement accuracy becomes inadequate. The A_{0-} wave modes around and beyond the coincidence frequency are almost unchanged as the properties of the loading fluid where the wave is supposed to travel are approximately the same as the depth changes. Only a slight shift toward higher frequencies of the deeply buried A_{0-} highest-order modes is detectable, which is in agreement with the slightly higher sand sound speed chosen to optimize the model-data fit for the deeply buried target with respect to the flush-buried case.

V. CONCLUSIONS

Measurements of elastic wave scattering from partially and completely buried spherical shells have been analyzed using a suite of wave theory target scattering models. The significance of burial depth was investigated by analyzing backscattering data from three identical spherical shells, respectively, half-, flush-, and completely buried within a sandy seabed. Free-field backscattering measurements obtained by suspending one of the spherical shells in the water column were used as a reference for verifying the geometry and the elastic parameters of the spherical shells, and as a benchmark for the target scattering models. With the objective of investigating the potential of using structural resonances for classification of buried targets, special emphasis was placed on investigating the excitation of the fundamental symmetric and antisymmetric Lamb-type waves (S_0 and A_0 , respectively).

The benchmark analysis of the backscattering from the free-field spherical shell demonstrated the capability of the scattering models to capture the dispersion characteristics of the A_0 and S_0 elastic components. On the other hand, the models consistently overestimated the scattered levels associated with the midfrequency enhancement of the antisymmetric modes, probably caused by shell imperfections or the presence of a lifting lug welded to the top of the spherical shells. The reflection from this top lug could also be identified in the data time series. A model-data mismatch was also detected at $f < 2$ kHz, common to all the data sets but particularly strong in the half-buried and flush-buried cases. The common effect may be due to a mismatch between the transmitted pulse and its model used in simulation. However, the greater discrepancy in the two cases mentioned remains unexplained.

Despite the low-frequency mismatch, the data analysis of the buried spherical shells showed good agreement between the measurements and theory,^{5,7,10} especially in terms of elastic wave dynamics. The elastic waves identified in the free-field case could be identified at all burial depths, and their dispersion characteristics were accurately represented by the models. As was the case for the free-field spherical shell, the level of the symmetric S_0 returns were accurately modeled as well, while the A_0 returns were overestimated in amplitude by the models. On the other hand the relative reduction of these arrivals relative to the half-buried spherical shell was accurately predicted. Due to their stronger interaction with the surrounding medium, the antisymmetric modes are more affected by burial into the sediment than the symmetric ones, an effect which is accurately captured by the models.

Another interesting result of the analysis is the independent confirmation of the strong dispersion of acoustic waves in a sandy seabed, recently demonstrated on the basis of acoustic data analysis by Maguer *et al.*¹⁵ Thus, the present analysis suggests a sediment sound speed of about 1640 m/s, whereas the direct core measurements at 200 kHz yielded 1720 m/s. As described in the earlier work, the Biot model was needed to interpret the experimental results.

The analysis of elastic wave scattering from the buried targets used in GOATS'98 is continuing. The analysis is con-

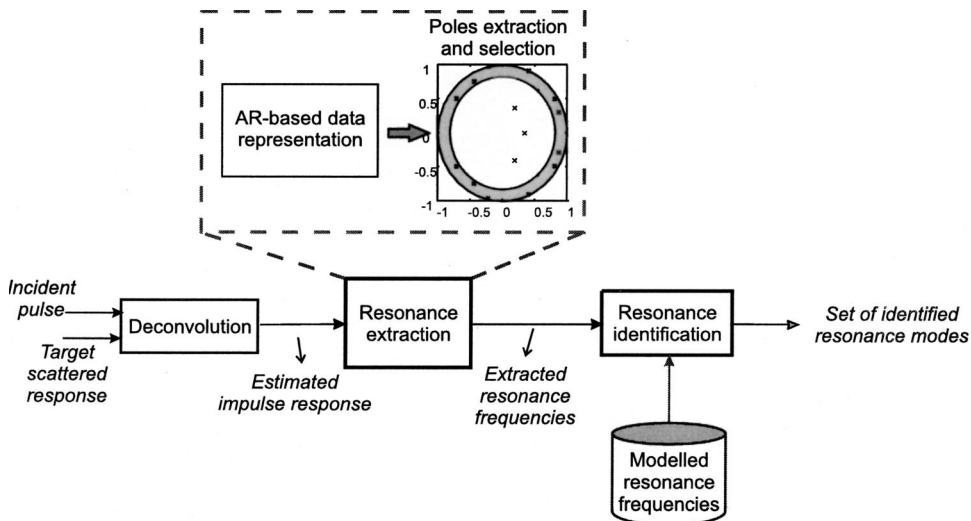


FIG. 16. Block diagram of the resonance extraction and identification procedure.

centrating on the subcritical insonification regime. Effective insonification below the critical grazing angle of the seabed would allow for higher area search rates, and low frequencies penetrate better into ocean sediments in these geometries. The analysis will be extended to the more complicated aspect-dependent scattering properties of buried cylindrical targets and bistatic receiver geometries.

ACKNOWLEDGMENTS

The authors wish to thank all the SACLANTCEN and MIT staff members involved in GOATS'98 experiment for their invaluable contribution to its success. They especially want to thank Per Arne Sletner for establishing and running the TOPAS source facility from the shore laboratory at Mariana Marina, and Marco Paoli for leading the extensive diving effort. Piero Guerrini excelled as Engineering Coordinator. The outstanding effort of the crews of R/V ALLIANCE and T/B MANNING is highly appreciated. The comments provided by Reginald Hollett contributed significantly to the quality of the paper and are highly appreciated. A special thanks to the Management at SACLANTCEN for squeezing GOATS'98 into their program of work at short notice, for their continued support for the entire project. The U.S. Office of Naval Research supported the MIT components of the experiment and the analysis is performed at the Coastal Systems Station.

APPENDIX: APPROACH OF RESONANCE FREQUENCY EXTRACTION AND MODEL-BASED IDENTIFICATION

The method used for extracting and identifying the elastic resonance modes from the measured response of a spherical shell is outlined in Fig. 16.

The approach used for the resonance extraction can be applied to any kind of elastic target. The identification method is model-based, with the reference model being the response of an air-filled, thin-walled spherical shell. However it can be extended to any other object, as long as a model is available.

The scatterer is assumed to be well represented by a linear time invariant (LTI) time-discrete system with a ratio-

nal transfer function (TF) model.^{1,18} Unattenuated resonances are defined as those poles of the TF of the LTI system that lie on the unit circle in the z domain. Furthermore, according to resonance scattering theory, the modal resonances have been proven to correspond to the poles of the rational transfer function of the scatterer.¹⁸ The most straightforward method for estimating the poles of a system consists of representing its TF with a parametric autoregressive (AR) model.³¹ As a real impulse response is to be modeled, all complex poles (or zeros) included in the TF rational pattern imply the presence of their respective complex conjugates among the poles (or zeros).¹

AR modeling is applied to the measured data after a preliminary nonparametric deconvolution of the target response which provides the impulse response of the scattering system. In theory, only the poles on the unit circle in the z plane are resonances of nondispersive waves. With the S_0 wave being almost nondispersive in the whole frequency range and the A_{0-} wave having relatively insignificant dispersion below the coincidence frequency, the corresponding modes are expected to lie within a finite annulus defined in the z plane. Each couple of complex conjugated poles and each real-valued pole estimated by the AR model which lies within the annulus is a potential resonance mode of the two waves. Here the $0.90 \leq |z| \leq 1$ annulus is assumed.

The set of resonance frequencies $\{f_k^{\text{AR}}, k = 1, \dots, K\}$ extracted from data are identified by the following model-based technique. A model pattern of expected resonance modes belonging to the A_{0-} and S_0 waves is numerically computed from the approximated formulas (9.4.9) and (9.4.13) presented in Ref. 32. This method was developed under free-field conditions,³² but has been adapted here to targets interacting with the seabed. The external sound speed and density required by the original algorithm are substituted with the effective quantities $c_{\text{ext}}^{\text{eff}}$ and $\rho_{\text{ext}}^{\text{eff}}$ defined in Sec. III B (see Ref. 29). This generalization is justified because of the contrast between the elastic properties of the target and the sediment which makes the effect of replacing water by sediment relatively insignificant in regard to the spectral locations of the modes, as confirmed by the results of the analysis.

The model produces a set of resonance frequencies

$$\{f_{l,n_l}, n_l=1,2,\dots,N_l, l \in L\}, \quad (\text{A1})$$

where l is the wave index ($L=\{S_0, A_{0-}\}$) and n_l is the resonance modal order of the l wave type. The AR-based extracted set of frequencies is identified by a simple algorithm of model-data pattern association.

The association problem is solved by a distance-based approach. The subset of measured resonances $\{f_{l,n_l}^{\text{AR}}, \hat{n}_l \in \{1, \dots, \hat{N}_l\}\}$ which best fits the model pattern [Eq. (A1)] is found for each wave type l in terms of minimum Euclidean distance between model-data pairs of frequencies:

$$\{f_{l,n_l}^{\text{AR}}\} = \{f_k^{\text{AR}} : \min_{k,n_l} (f_k^{\text{AR}} - f_{l,n_l})^2 < \text{thr}\}. \quad (\text{A2})$$

Hence, for the l wave type, if the distance between the measured frequency f_{k*}^{AR} and a certain modeled resonance mode f_{l,n_l*} is the minimum over all the n_l values, but is higher than a fixed threshold thr , then f_{k*}^{AR} cannot be identified with any of the resonance modes predicted for the l wave.

- ¹A. Tesei, W. L. J. Fox, A. Maguer, and A. Løvik, "Target parameter estimation using resonance scattering analysis applied to air-filled, cylindrical shells in water," *J. Acoust. Soc. Am.* **108**, 2891–2900 (2000).
- ²C. E. Baum, "Discrimination of buried targets via the singularity expansion," *Inverse Probl.* **13**, 557–570 (1997).
- ³A. Maguer, W. Fox, H. Schmidt, E. Pouliquen, and E. Bovio, "Mechanisms for subcritical penetration into a sandy bottom: Experimental and modeling results," *J. Acoust. Soc. Am.* **107**, 1215–1225 (2000).
- ⁴H. Schmidt, and J. Lee, "Physics of 3-d scattering from rippled seabeds and buried targets in shallow water," *J. Acoust. Soc. Am.* **105**, 1605–1617 (1999).
- ⁵R. Lim, J. L. Lopes, R. H. Hackman, and D. G. Todoroff, "Scattering by objects buried in underwater sediments: Theory and experiment," *J. Acoust. Soc. Am.* **93**, 1762–1783 (1993).
- ⁶J. A. Fawcett, "Summary of object/waveguide scattering modeling at SACLANTCEN (1995–1998)," SR-298, NATO SACLANT Undersea Research Centre, La Spezia, Italy, June 1998.
- ⁷R. Lim, "Scattering by partially buried shells," in *Proceedings of the ICA/ASA Meeting* (AIP, New York, June 1998), Vol. 1, pp. 501, 502.
- ⁸H. Schmidt, A. Maguer, E. Bovio, W. Fox, K. LePage, N. Pace, P. Guerini, P. Sletner, E. Michelozzi, B. Moran, and R. Grieve, "Generic oceanographic array technologies (GOATS)'98-Bi-static seabed scattering measurements using autonomous underwater vehicles," SR-302, NATO SACLANT Undersea Research Centre, La Spezia, Italy, October 1998.
- ⁹I. A. Viktorov, *Rayleigh and Lamb Waves. Physical Theory and Applications* (Plenum, New York, 1967).
- ¹⁰G. S. Sammelmann, D. H. Trivett, and R. H. Hackman, "The acoustic scattering by a submerged, spherical shell. I. The bifurcation of the dispersion curve for the spherical antisymmetric Lamb wave," *J. Acoust. Soc. Am.* **85**, 114–124 (1989).
- ¹¹M. Talmant, H. Überall, R. D. Miller, M. F. Werby, and J. W. Dickey, "Lamb waves and fluid-borne waves on water-loaded, air-filled thin spherical shells," *J. Acoust. Soc. Am.* **86**, 278–289 (1989).
- ¹²O. Bergem, and N. G. Pace, "Calibration of the TOPAS PS040. I. Mea-

surements recorded with TOPAS acquisition system," SM-119, NATO SACLANT Undersea Research Centre, La Spezia, Italy, Jan. 1996.

- ¹³D. J. Wingham, N. G. Pace, and R. V. Ceen, "An experimental study of the penetration of a water-sediment interface by a parametric beam," *J. Acoust. Soc. Am.* **79**, 363–374 (1986).
- ¹⁴E. Breitenbach, H. Überall, and K.-B. Yoo, "Resonant acoustic scattering from elastic cylindrical shells," *J. Acoust. Soc. Am.* **74**, 1267–1273 (1983).
- ¹⁵A. Maguer, E. Bovio, W. Fox, and H. Schmidt, "In situ estimation of sediment sound speed and critical angle," *J. Acoust. Soc. Am.* **108**, 987–996 (2000).
- ¹⁶J. A. Fawcett, W. L. J. Fox, and A. Maguer, "Modeling of scattering by objects on the seabed," *J. Acoust. Soc. Am.* **104**, 3296–3304 (1998).
- ¹⁷E. A. Robinson, and S. Treitel, *Geophysical Signal Analysis* (Prentice-Hall, Englewood Cliffs, NJ, 1980).
- ¹⁸N. D. Veksler, *Resonance Acoustic Spectroscopy* (Springer, Berlin, 1993).
- ¹⁹K. F. Graff, *Wave Motion in Elastic Solids* (Dover, New York, 1991).
- ²⁰S. G. Kargl, and P. L. Marston, "Observations and modeling of the back-scattering of short tone bursts from a spherical shell: Lamb wave echoes, glory, and axial reverberations," *J. Acoust. Soc. Am.* **85**, 1014–1028 (1989).
- ²¹G. Maze, F. Leon, J. Ripoche, and H. Überall, "Repulsion phenomena in the phase-velocity dispersion curves of circumferential waves on elastic cylindrical shells," *J. Acoust. Soc. Am.* **105**, 1695–1701 (1999).
- ²²A. D. Pierce, *Acoustics. An Introduction to its Physical Principles and Applications* (ASA, New York, 1989).
- ²³F. Magand, and P. Chevret, "Time frequency analysis of energy distribution for circumferential waves on cylindrical elastic shells," *Acust. Acta Acust.* **82**, 707–716 (1996).
- ²⁴A. Boström, "Scattering of stationary acoustic waves by an elastic obstacle immersed in a fluid," *J. Acoust. Soc. Am.* **67**, 390–398 (1980).
- ²⁵A. Boström, "Scattering of acoustic waves by a layered elastic obstacle in a fluid-An improved null field approach," *J. Acoust. Soc. Am.* **76**, 588–593 (1984).
- ²⁶R. Lim, "Acoustic scattering by a partially buried three-dimensional elastic obstacle," *J. Acoust. Soc. Am.* **104**, 769–782 (1998).
- ²⁷A. Boström, "Multiple scattering of waves by bounded obstacles," *J. Acoust. Soc. Am.* **67**, 399–413 (1980).
- ²⁸B. Peterson, V. K. Varadan, and V. V. Varadan, "Scattering of elastic waves by a fluid inclusion," *J. Acoust. Soc. Am.* **73**, 1487–1493 (1983).
- ²⁹If a wave diffracts around the partially buried sphere in a time t at speeds in each medium not too far from the external sound speeds in these media, then we can assume $t \approx (L_w/C_w) + (L_s/C_s) = L/c_{\text{ext}}^{\text{eff}}$. Here, L_w is the path length around the sphere in water, L_s is the path length around the sphere in sediment, $L = L_w + L_s$, C_w is the water sound speed, C_s is the sediment sound speed, and $c_{\text{ext}}^{\text{eff}}$ is the effective speed. Then $c_{\text{ext}}^{\text{eff}}$ could be solved for as $c_{\text{ext}}^{\text{eff}} = L/(L_w/C_w + L_s/C_s)$.
- ³⁰G. Kaduchak, C. S. Kwiatkowski, and P. L. Marston, "Measurement and interpretation of the impulse response for backscattering by a thin spherical shell using a broad-bandwidth source that is nearly acoustically transparent," *J. Acoust. Soc. Am.* **97**, 2699–2708 (1995).
- ³¹S. M. Kay, *Modern Spectral Estimation: Theory and Application* (Prentice-Hall, New York, 1988).
- ³²J. D. Kaplunov, L. Y. Kossovich, and E. V. Nolde, *Dynamics of Thin Walled Elastic Bodies* (Academic, San Diego, 1998).
- ³³P. Marston, and N. Sun, "Resonance and interference scattering near the coincidence frequency of a thin spherical shell: An approximate ray synthesis," *J. Acoust. Soc. Am.* **92**, 3315–3319 (1992).